Full Length Article

A closed loop system to control transverse deformations in LHC collimators

Thomas Furness [a],[*], Simon Fletcher [a], James Williamson [a], Haydn Martin [a], Stefano Redaelli [b], Federico Carra [b], Alessandro Bertarelli [b], Michele Pasquali [c]

[a] *The University of Huddersfield, Queensgate, Huddersfield, HD13DH, UK*
[b] *CERN, Espl. des Particules 1, 1211, Meyrin, Switzerland*
[c] *Sapienza University of Rome, Piazzale Aldo Moro 5, 00185, Rome, Italy*

ARTICLE INFO

ABSTRACT

This work presents a novel closed-loop control system for the detection and control of thermal deformations integrated in the secondary collimators of the Large Hadron Collider (LHC). Interactions between spurious particles lost transversally from the circulating beam core and the collimator jaws that make up the active area of the collimator will result in thermally induced deformations in those jaws. This interaction can push the jaw's straightness out of the tolerance and force the jaw either into the beam core or away from it. This action can result in reductions in beam cleaning efficiency and increases in impedance on the beam. Whilst deformations in either direction are to be avoided, deformations into the beam are considered more of an issue as too much deformation can provoke beam dumps if beam losses are too high. To minimize this unavoidable thermal effect a novel adaptive closed-loop monitoring and actuation system, comprising of multiple intrinsic Fabry–Pérot interferometric (IFPI) optical sensors, and several integrated piezoelectric stack actuators, has been developed. When operating, this system can transiently monitor the jaws straightness and when required correct for deformations up to 500 μm. In addition, subsequent steps to use this system as an active damper to reduce vibratory response, as experienced when the jaw undergoes a direct beam impact, are also discussed.

1. Introduction

The nominal luminosity of the LHC requires the storage and collision of two 7 TeV beams each with 360 MJ of potential energy [1]. During last LHC run in 2015–2018, the LHC operated at 6.5 TeV and exceeded already 300 MJ of beam stored energy. In the coming years this is set to increase with the advent and implementation of the high luminosity upgrade (HL-LHC), increasing the stored energy of the beams to 680 MJ [2]. At these levels, even a small loss can cause major damage or magnet quenching, potentially resulting in downtime and, in the worst case, costly repairs. As such, losses are limited to as little as tens of mJ/cm^3 and 1 J/cm^3 for magnet quenching and material damage, respectively [3]. To maintain these limits and ensure machine safety the LHC employs numerous protection systems, chief amongst which is the collimation system. The LHC's collimation system is a passive three-tiered system, comprising of primary, secondary, and tertiary collimators, presented in various geometrical configurations located around the LHC's orbit [4]. Whilst each tier of the collimation system performs a specific role with respect to beam cleaning, broadly, the design of each collimator is geometrically similar. Each collimator consists of two "jaws" that straddle the beam. These jaws may be presented horizontally, vertically, or skewed to ensure full coverage

around the beam. The main area of the jaws is the active longitudinal absorption areas, which in primary and secondary collimators consists of several blocks of a low-Z material such as carbon fiber re-enforced carbon, or more recently molybdenum carbide graphite [2]. Materials like these are chosen due to the low number of protons in their nuclei, making them robust absorbers for the collimator's jaws. However, the use of materials such as the ones mentioned above can lead to higher induced impedance on the circulating beam. These blocks are then clamped in an oxygen-free dispersion strengthened copper housing, integrated into which is a dedicated cooling system capable of evacuating the high heat loads generated by loss absorption [5]. These jaws are then housed in a vacuum tank and are connected to an actuation system with two motors per jaw that can position the jaws transversally along the collimation plane (horizontal, vertical, or skew) and adjust their tilt angle with respect to the beam. An example of the HL-LHC secondary collimator for HL-LHC is shown in Fig. 1.1 [6]. The work by *A. Bertarelli et al.* [4,7], provides a more in-depth review regarding collimator design. During nominal operation, the circulating beam core transits about 11 000 times per second though the aperture created by the placement of the collimator's two jaws. As the beam passes though the primary collimator the primary halo is intercepted by the jaw's absorption area. A fraction of it is out scattered into a
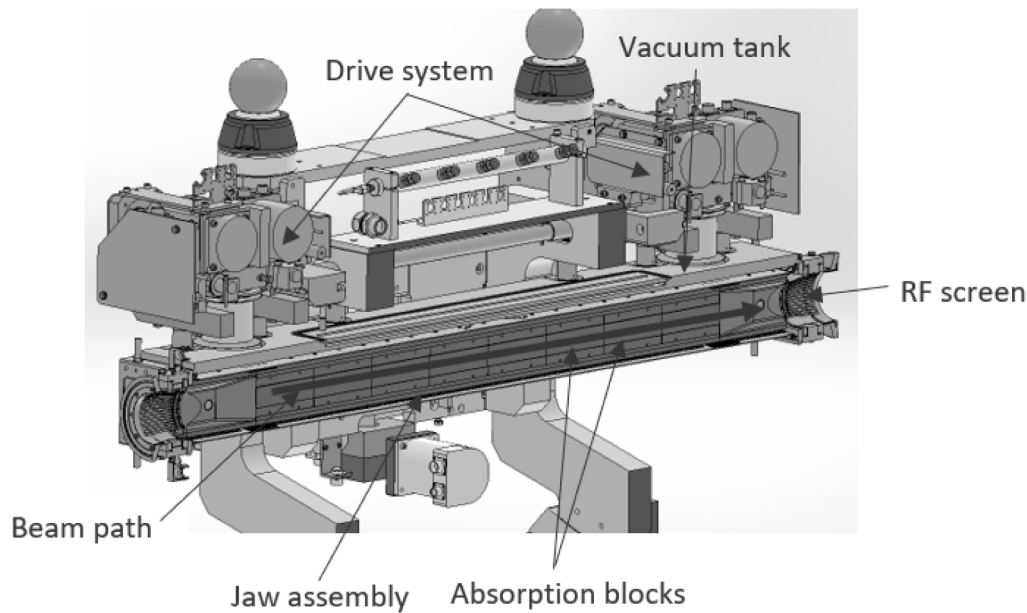

Fig. 1.1. Section view of the HL-LHC secondary collimator.

secondary halo which is then intercepted further downstream by the secondary collimator in the multi-turn process. Here, most protons are absorbed, but certain spurious particles can escape to form a tertiary halo, which is in turn intercepted by tertiary collimators if that is deemed necessary [8]. During interception large amounts of energy are deposited into the jaws generating high heat loads. Whilst each jaw does have its own dedicated cooling system which under nominal operation allows each jaw to be thermally balanced, exceptional events can induce additional thermal inputs that can displace the jaws thermal equilibrium, and in turn induce thermal deformations affecting the jaws straightness.

1.1. Thermal deformations and jaw straightness tolerances

To ensure that beam cleaning efficiency is optimum, the maximum admissible straightness error for each jaw is ± 100 μm over the 1.0 m length of the active surface [9] with respect to the beam. Several aspects of the current jaw's design ensure that the during nominal operation the jaws do not exceed this threshold. Their robust mechanical design ensures that collimator jaws can withstand their fundamental operation, and cope with nominal beam losses. The jaws are designed to be inherently stiff, and as previously mentioned, the dedicated cooling system can evacuate the high heat loads generated by particle absorption limiting thermal deformation. In addition, jaw block flatness and mechanical errors associated with the assembly of the jaw that can add to the overall jaw straightness error, are minimized though precise manufacturing and multiple inspections during the assembly process. Angular misalignment of the jaw with respect to the beam can be corrected to certain degree through the precise control of the collimator drive system [10], shown in Fig. 1.1. However, outside of nominal operations, larger transverse thermal deformation generated by abnormal losses, are much more difficult to detect and resolve.

1.2. Loss effect on collimator jaws

The loss effect scenarios to be considered in this work can be partitioned into two areas: (1) slow quasi-static losses, generating elastic thermal deformations, and (2) direct beam impacts (dynamic losses) generating vibratory dynamic responses potentially resulting in plastic deformations [6,11,12]:

- Quasi – static losses
    1. Steady state – 1 h beam lifetime (BLT), 1.68e11 p/s at 7 TeV are lost at the primary collimators leading to a 9.38 kW energy disposition on the most loaded secondary collimator jaw
    2. Accidental state – 0.2 h BLT, 8.34e11 p/s at 7 TeV are lost at the primary collimators leading to 46.9 kW on the most loaded secondary collimator jaw

- Dynamic losses
    1. Injection error with a full injected train of 288 bunches at 450 GeV impacts the jaw.

To understand how the above beam loss scenarios interact with the mechanical design of the jaws with regards to displacement magnitude and direction, the work of *F. Carra et al.* [13] and *M. Cauchi et al.* [14,15] was reviewed and a new set of finite element thermomechanical simulations were created. To begin, the numerical analysis energy deposition maps relating to the abovementioned scenarios were obtained from CERN. The energy deposition maps are generated by the Monte Carlo based code FLUKA [16]. By simulating the shower effects on the jaw's geometry, the FLUKA code can provide the spatial energy distribution across the geometry for each of the defined scenarios [14]. The outputted energy distribution is given in GeV/cm^3/p but using dedicated Ansys® parametric design language (APDL) in the finite element analysis (FEA) software, this energy deposition can be transposed into a thermal load by means of power density distribution. With the energy distribution now importable as a thermal load, thermomechanical simulations generated in ANSYS® were created to determine the jaws geometrical response when subjected to these energy depositions.

Fig. 1.2 shows the meshed CAD model of the secondary collimator jaw. The jaw has a fixed support at one end but is allowed to rotate around that fixed support. At the other end, a cylindrical support allows the model to rotate but also move laterally in the X direction (according to Fig. 1.2). This system replicated the way the jaw is held under real operation. In addition, a convention coefficient of 13 8000 W/m^2 K was applied to the geometry representing the jaw's cooling circuit (not shown).

First, the thermal loads representing the quasi-static losses, were simulated. Fig. 1.3 (1) shows the temperature distribution from a 9.38 kW steady-state energy deposition, resulting in a max temperature of 126.77 °C, and a max induced thermal deformation of 68.4 μm
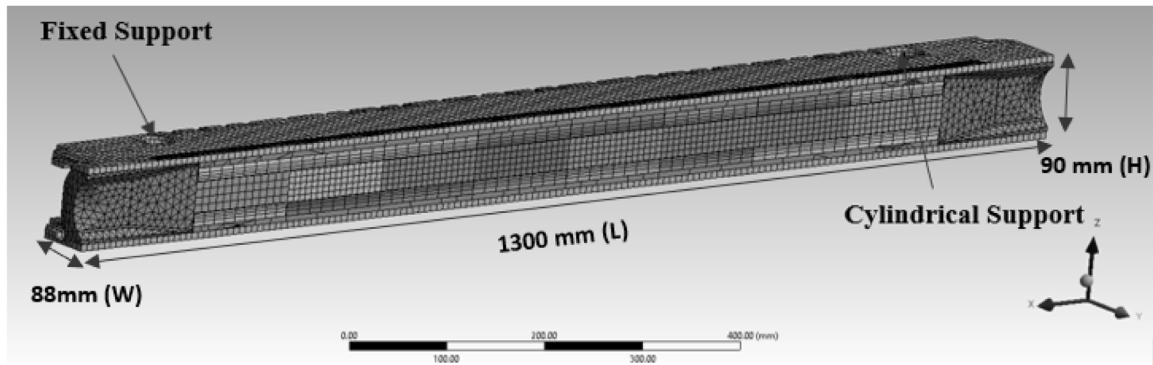
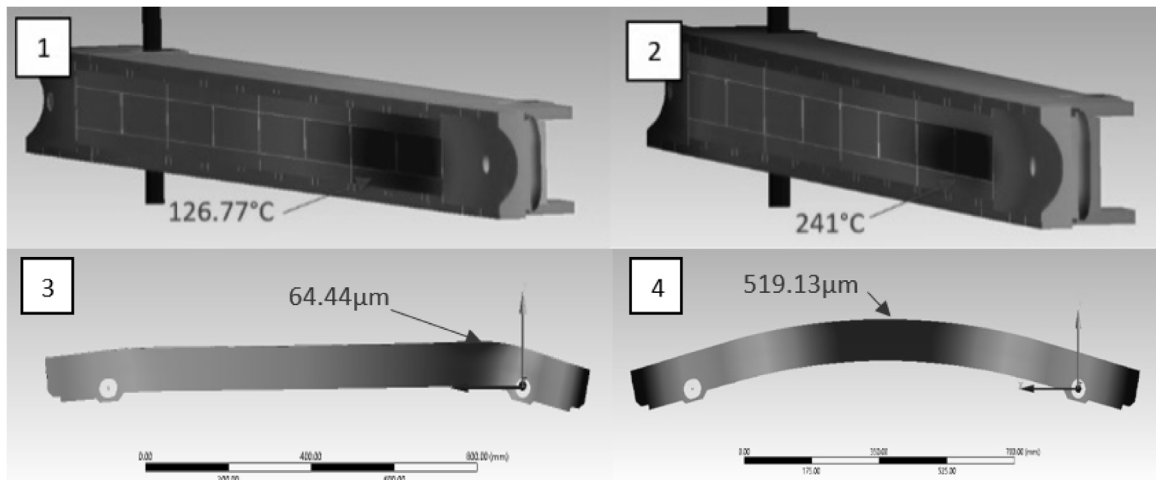**Fig. 1.2.** Set up of the secondary jaw meshed model in Ansys®.

Fig. 1.3. (1) Thermal Distribution from 9.38 kW energy deposition, (2) Thermal Distribution from 46.9 kW energy deposition (3) resultant thermal deformation from 9.38 kW (4) resultant thermal deformation from 46.9 kW.

(Fig. 1.3 (3)). Fig. 1.3 (2) shows the temperature distribution from a 46.9 kW energy deposition, resulting in a max temperature of 241 °C, and a max induced thermal deformation of over 0.5 mm (Fig. 1.3 (4)). The resultant jaw profiles from these induced thermal deformations are shown in Fig. 1.4. These results show a thermally induced elastic deformation of more than 0.5 mm. Given that these deformations are elastic, they will return to their nominal position over time after the additional heat load is removed. However, as stated before the induced straightness error can lead to beam instabilities within that time frame.

In addition to the quasi-static simulations performed above, a dynamic loss simulation was also performed to ascertain the vibratory response the jaw is subjected to after such an event has occurred. Fig. 1.5 shows the vibratory response over 1 s, after a 450 GeV 288 bunch train, like that observed during an SPS injection error event, has impacted the jaw. As can be seen in Fig. 1.5, such a beam impact event induces a large vibratory response (≈60 Hz) with amplitudes of more than 2 mm.

Whilst direct beam impact events such as the one simulated above are yet to occur in the LHC proper and have only been physically tested in dedicated beam tests [17], such an impact could plastically deform the jaw, which given the sealed collimator environment would lead to permanent jaw deformity in terms of jaw straightness.

2. Adaptive collimator system (ACS) design

In attempts to control these jaw deformations, a closed-loop controlled adaptative collimator is proposed. This proposed system consists of three main area of interest:
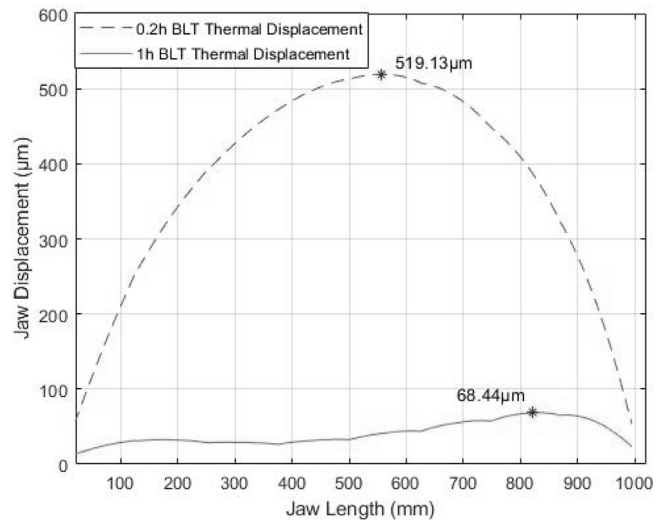

Fig. 1.4. Thermal deformation profile.

1. A measurement system mounted directly onto the jaws body to allow the real-time monitoring of the jaws form, and more importantly any perturbations that may arise from beam interactions.
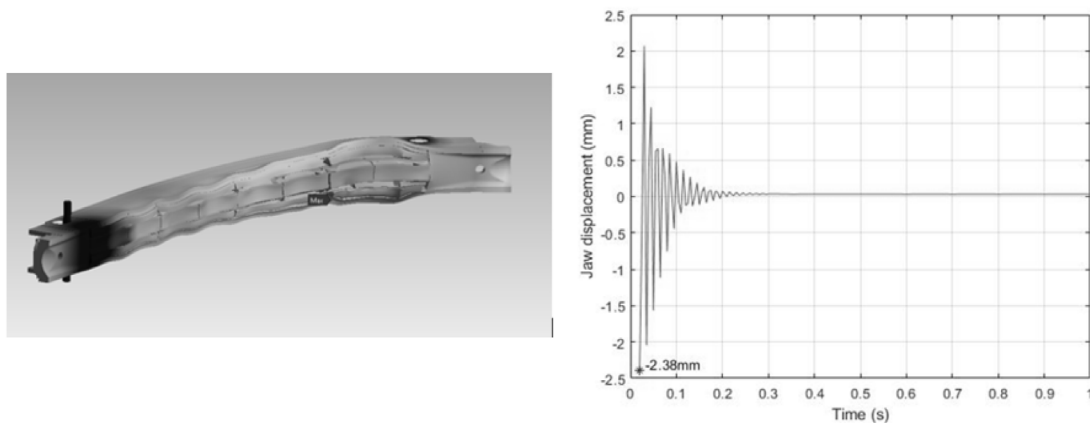
Fig. 1.5. (R) Jaw vibratory response after 440 GeV 288 bunch beam impact, (L) FEA deformation response.
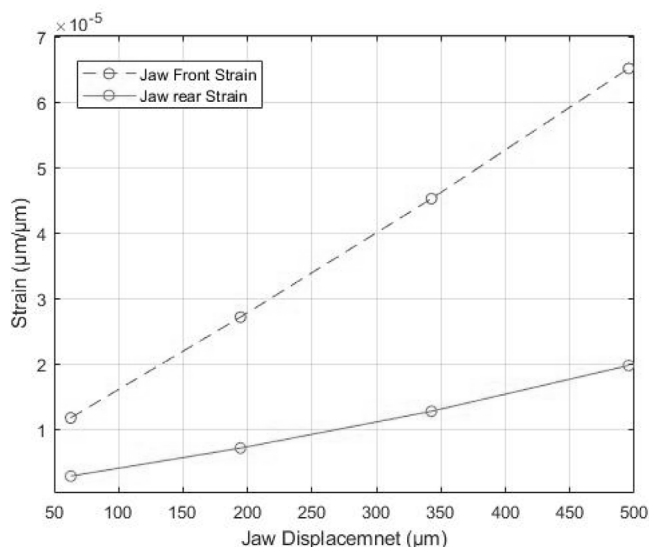

Fig. 2.1. Jaw front and rear strain results verses jaw deformation.

2. An actuation system that can generate enough force to correct for jaw deformations and can actuate fast enough to potentially damp vibratory responses.

3. A high-speed control loop that will receive the jaw measurement data and generate corrective proportional output responses that can be sent to an actuation system.

2.1. Fiber optical strain measurement

Given the current design of a typical secondary collimator, direct displacement measurement would not be possible due to size limitation inside the vacuum tank (Fig. 2.6), and the lack of a reference point on the jaws themselves. Therefore, mounted on the jaw directly, a differential strain-based system would be used to determine jaw deformation and magnitude.

From the FEA simulations of jaw deformations, Fig. 2.1 shows that there is a definitive difference between the strain at the front of the jaw and at the rear. It shows that a 500 μm transverse displacement generates a differential 45 $\mu\varepsilon$.

An early form of strain measurement that was envisaged for this operation was a series of slotted photomicrosensor based on the work of *Potdar et al.* [18]. Whilst these sensors had an acceptable linear measurement range, coupled with high resolution suitable for this application, their lack of radiation tolerance [10] and the potential bulky design prohibited there use in the final adaptive collimator design.

To overcome these issues a new fiber optical strain measurement system was conceived that would be resilient to electromagnetic radiation and presented a smaller physical package which would allow for better integration into the new collimator design. This optical system utilized spectral interferometry and a series of strain sensitive intrinsic Fabry–Perot interferometer (IFPI) probes, resulting in an absolute strain measurement system, based upon the work of *Williamson et al.* [19]. This new measurement option was desirable as it would allow for the integration of more sensors giving a greater spatial coverage of the jaws body. It would also allow for a long sensor gauge length that would allow for higher stain resolution, <100 nε, more than adequate for this application.

Fig. 2.2 shows the optical layout of the system. Light from a broadband ($\lambda C = 850$ nm, $\Delta\lambda = 50$ nm) super luminescent diode enters a 2×2 fiber optic coupler. Then a 1×8 fiber switch allows the selection of the active fiber strain gauge and hence time division multiplexing of the strain signal. From the fiber switch, the source light travels along 5 m lengths of single mode fiber (780 HP), through an 8×8 FC/APC vacuum port (not shown) into the collimator vacuum tank and along the collimator jaws to the fiber strain gauges (D1 and D2) [10]. A complete description of this system and its operation can be found in [19], with [10] detailing how this system integrates into this work. [10] also details the work undertaken to construct and integrate the IFPI probes. This includes the coating of the probes in titanium oxide/silicon dioxide, to improve signal attenuation, and the steps taken to reduce the effects of the anticipated ionizing radiation fiber darkening.

The final ACS design envisaged the incorporation of six 150 mm IFPI probes in two tracks, three in the front track and three in the rear track (locations shown in Fig. 2.3).

Incorporating the fibers in this way makes three differential pairs, allowing for both magnitude and direction to be determined based on the differential value of the two paired strain measurements. Whilst the initial design had postulated six differential pairs of IFPI probes, mounting the optical probes proved more difficult than was first thought.

Initial bench tests had the IFPI probes epoxied to the body of the jaw. For the initial evaluation this was acceptable. Bonding the fibers in this way allowed for the probes and their corresponding patch cables to be grouped together in pre-machined recesses then covered in the epoxy, firmly fixing them in place. However, for the actual prototype the IFPI probes would have to be mechanical clamped to the jaw's structure due to the forbiddance of epoxies and other glues in the LHC's ultra-high vacuum environment as their inclusion would lead to unacceptable outgassing rates. To alleviate this issue the IFPI probes were clamped into two custom designed mounts that were then bolted to the positions shown in Fig. 2.3. The clamps needed to be finely balanced between clamping the IFPI probes firmly so that no slippage occurs, and that strain transfer is optimal, but not exert so much clamping force that the probes are crushed. This clamp design is
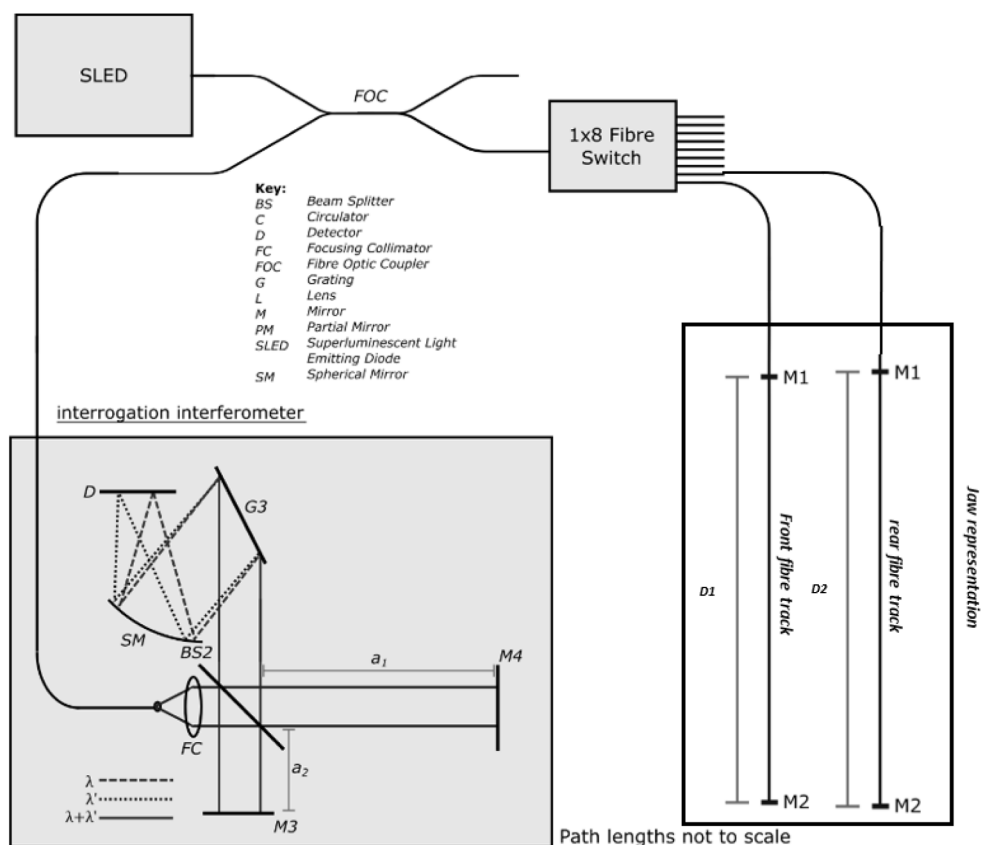
Fig. 2.2. Schematic of optical layout of the strain sensitive IFPI and remote interrogation, (*curtesy of T. Furness et al.* [9]).
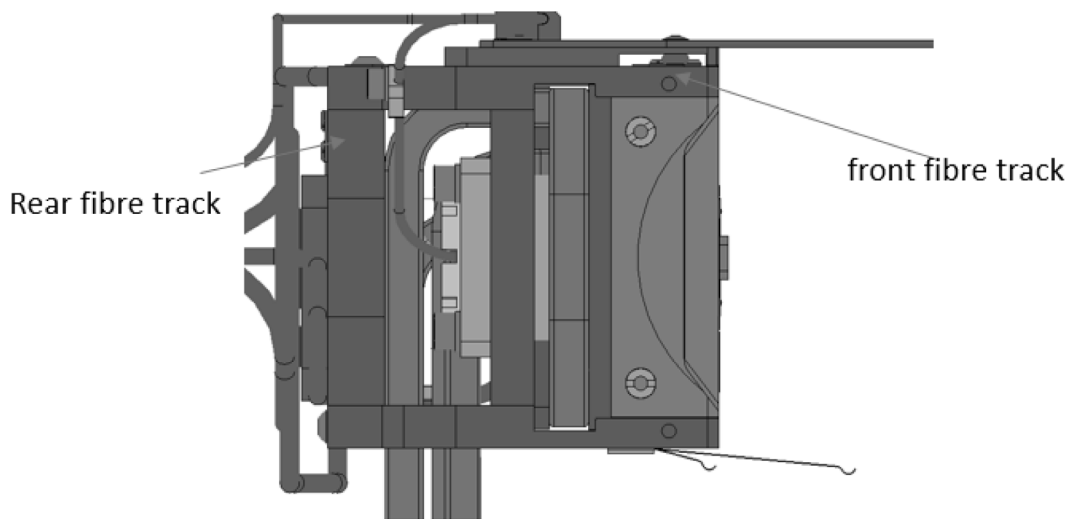

Fig. 2.3. End view of the collimator jaw showing front and rear fiber track placement (Curtesy of *T Furness et al.* [10]).

shown in Fig. 2.4. Whilst this design did allow for the IFPI probes to be mounted onto the jaw, without the use of glues, incorporating six fibers per track into each clamp proved difficult due to the size of the recess needed to clamp each fiber, and the space available to integrate the fiber track into the jaw's structure. Ultimately the number of IFPI probes per track was reduced to three. Whilst this did reduce the overall spatial strain coverage of the jaw, it was adequate to observe first order displacements, the type as seen in Fig. 1.3.

2.2. PZT actuation

As seen in Fig. 1.4 the maximum displacement the jaw undergoes during slow-loss beam interactions reviewed in this work is 519 μm. To correct this displacement a series of high powered piezo-ceramic (PZT) actuators were incorporated into jaws body. The actuators used were specialized PI ceramic® P.025-80P stack actuators (specification in Table 2.1). PZTs were used over other alternatives due to the large force
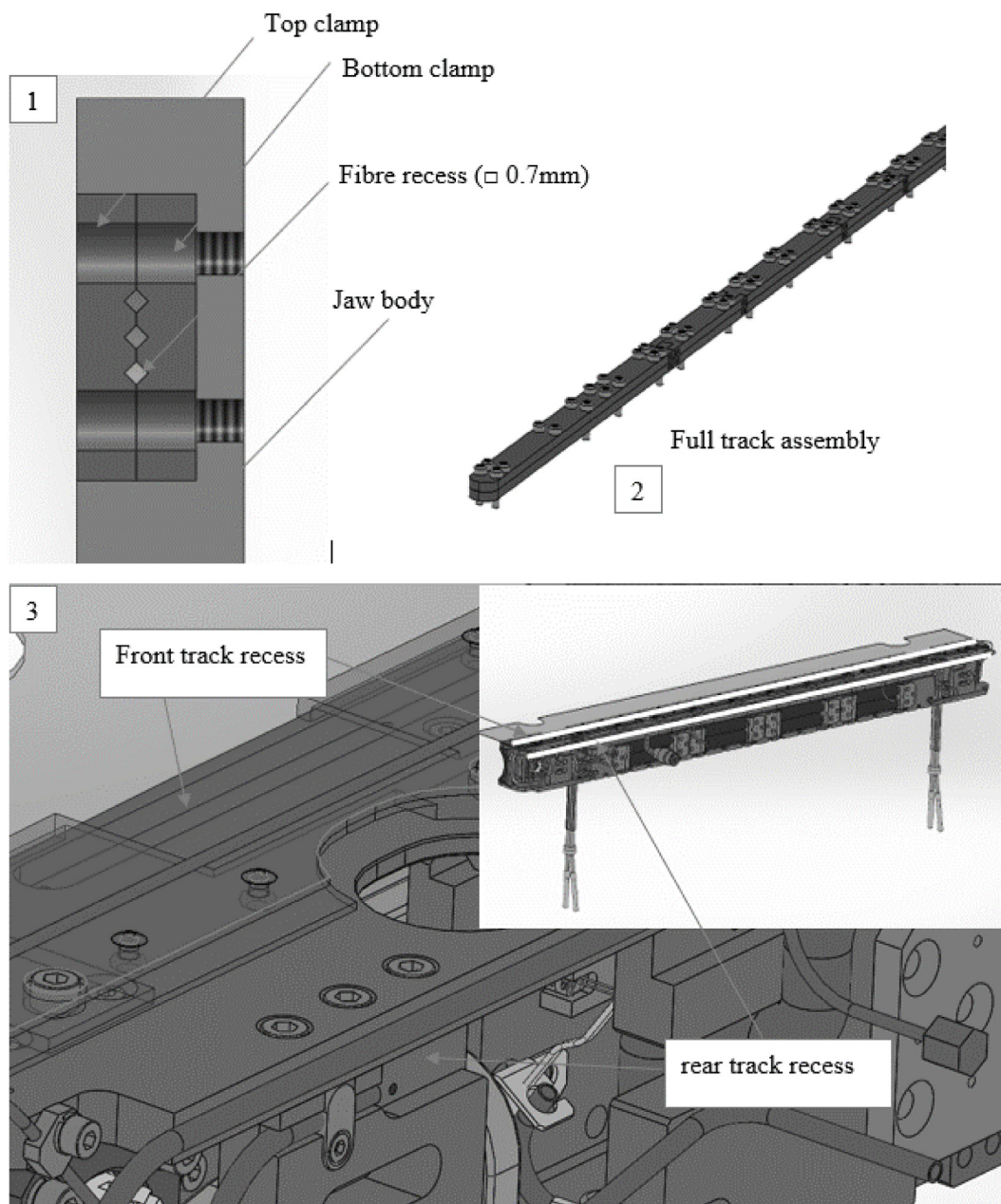
Fig. 2.4. (1): cross section of the IFPI probe clamp, (2): the full fiber track assembly, (3): the main jaw body showing the recesses for the fiber tracks, and placement along the full jaw length (highlighted in white).

Table 2.1
P.025-80P specification.

Max displacement @ 1000 V	120 μm
Diameter OD	25 mm
Length L	165 mm
Blocking force (F_b)	14,000 N
Stiffness K	120 μm/N
Capacitance	2600 nF
Resonant frequency	10 KHz
Ceramic type	PIC 255
Operating Temp T	−20 to 150 °C
Operating voltage V	0–1000 V

generation they can provide (to correct the slow loss displacements), but also for the fact that they have extremely fast raise times, which will be necessary for vibratory damping in the frequency of interest to be achieved.

Through numerous design iterations, it was determined that for a 500 μm corrective movement eight of these actuators would need to be incorporated into the jaw design to generate a sufficient corrective force. The huge force required to displace the jaw through that range is mainly down to the initial jaw being designed to be inherently very stiff. Additionally, also due to the limited space inside the jaw's vacuum tank these actuators needed to be placed by necessity, very close the jaws geometric neutral plane.

Fig. 2.5 shows the new ACS actuator design embedded into the rear of the jaw structure. To accommodate this the standard rear jaw stiffener was removed and replaced with a modular housing that could enclose the eight PZTs. Whilst the next size up of PZT from PI® could generate the necessary force requirements, space constraints inside the vacuum tank meant that the larger diameter of PZT could not be used. As shown in Fig. 2.6 when the jaws are in their parked position there is only a 25 mm between the jaw and tank wall. Additionally, the tank
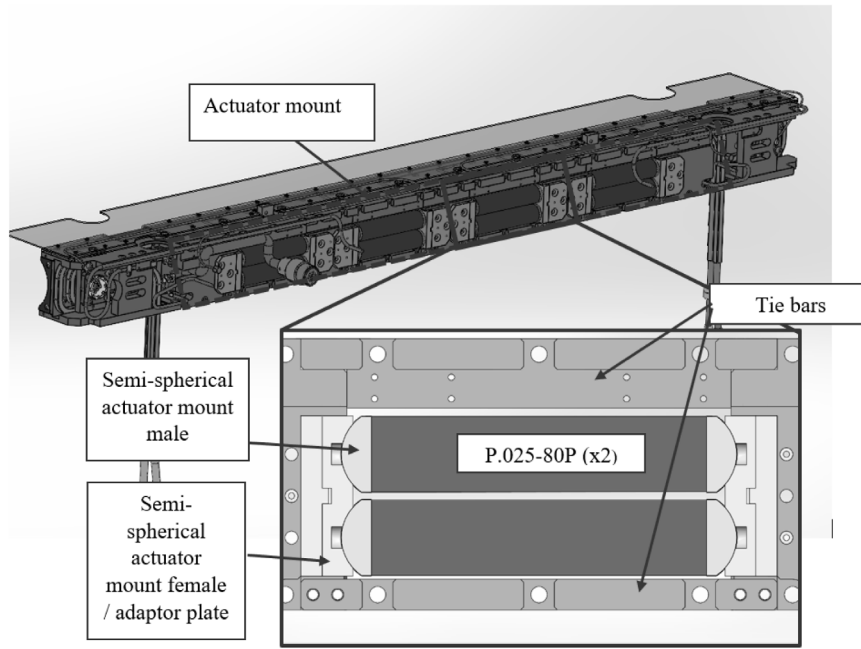
Fig. 2.5. Actuator mount in rear of jaw with a superimposed cross section view of the mounted actuators.
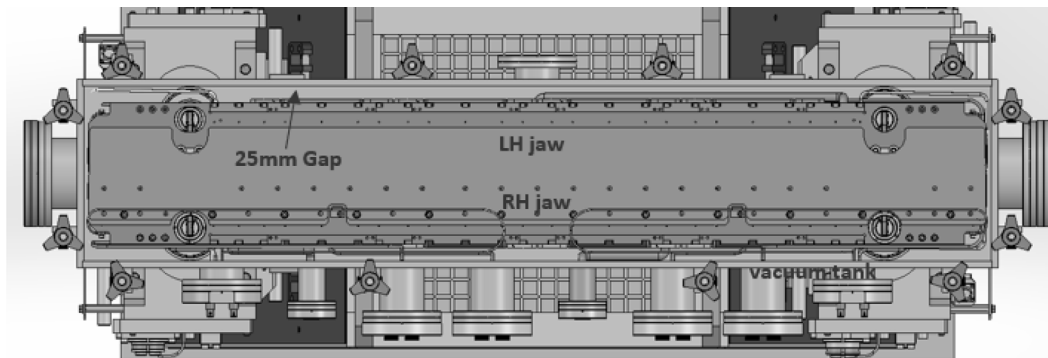

Fig. 2.6. Top view cross section on the collimator showing size constraints inside the vacuum tank.

itself cannot be enlarged due to size constants with respect to other LHC hardware potentially located near the collimator.

Therefore, to ensure adequate force generation each pair of the smaller PZT acts in union, with a combined blocking force generation of 28 kN. Each PZT was supplied with a semi-spherical end cap which allowed it, once mounted into the female adaptor plate, to rotate freely negating any lateral torsion that could be subjected onto the PZT during jaw displacement. One issue with the mounting of the PZTs was that across the sixteen PZTs acquired their overall length could vary within ±0.5 mm. To ensure a rigid fit between the PZT and the mount, each adaptor plate was machined oversize with added locating features and extra relief. Designing the actuator mount in this way meant that during the final assembly each adaptor plate could be re-machined down to suit the differing lengths of PZT. Once situated in the adaptor plates, the tie bars, which were designed undersize, would pull the adaptor plates together ensuring no gaps would be present between the PZTs and there corresponding mounts. If gaps did exist in the assembly, when actuated the PZT would first fill those gaps before contacting the adaptor plate, thus reducing force generation. The design seen in Fig. 2.5 was introduced back into ANSYS® and subjected to the same thermo-mechanical simulations as seen in Fig. 1.3. In addition to the boundary conditions already described, additional electro-mechanical conditions were set using ANSYS's *Piezo and MEMS* add-on. Table 2.2 shows the additional

Table 2.2

Mechanical and dialectic constant for PIC255 [20].

Density (kg/m^3)	7800
Youngs modulus (X direction) (Pa)	6.2e10
Youngs modulus (Y direction) (Pa)	6.2e10
Youngs modulus (Z direction) (Pa)	2.6e10
Passion's ratio (X direction)	0.3
Passion's ratio (Y direction)	0.3
Passion's ratio (Z direction)	0.3
Shear modulus XY (Pa)	2.4e10
Shear modulus YZ (Pa)	2.4e10
Shear modulus XZ (Pa)	2.4e10
Relative permittivity ε_{11}	1750
Relative permittivity ε_{33}	1800
Piezoelectric voltage coefficient g_{31} (Vm/N)	−10.1e−3
Piezoelectric voltage coefficient g_{33} (Vm/N)	25e−3
Piezoelectric voltage coefficient g_{15} (Vm/N)	38.4e−3
Cross voltage (V)	1000

mechanical properties for the material representing the PZTs, which in this case is *PI Ceramics* modified lead zirconate titanate (PIC255).

With the above mechanical and dielectric constants inputted into the new FEA model, the 0.2 h BLT simulation shown in Fig. 1.3 were rerun with both the thermal load representing the beam losses and the newly inputted PZT resistive force consisting of all eight PZTs, each
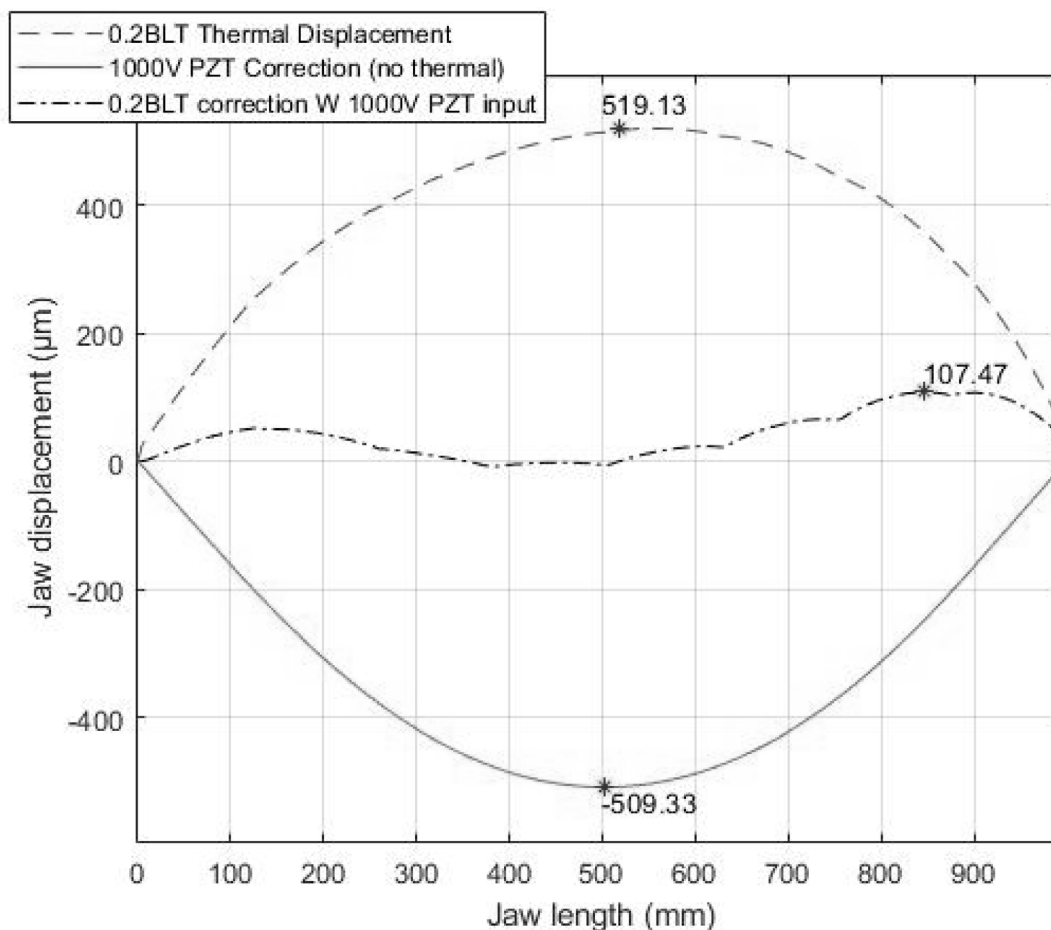
Fig. 2.7. FEA jaw displacement results, showing jaw form with and without PZT correction.

with 1000 V going across them. The simulation results are shown below in Fig. 2.7. As can be seen, the thermal energy generated from a 0.2 h BLT event causes the jaw to deform by over 500 µm in the positive direction. However, when all eight PZT now mounted in the rear of the jaw structure are energized by passing 1000 V across them, the deformation is reduced by almost a factor of five, bringing the majority of the jaw's centerline back under the 100 µm upper tolerance threshold.

Additionally, the maximum deformation the PZTs can generate alone (i.e., with no additional thermal input) is also shown in Fig. 2.7.

The 2D profiles shown in Fig. 2.7 are all taken from the jaw absorber center line on the front face. Whilst most of the corrected jaw profile seen in Fig. 2.7 has been reduced to below the 100 µm limit, as can be seen the maximum value is in fact still higher than that limit. By taking additional 2D profiles above and below this center line it is observed that whilst the absorber center line is higher than the 100 µm limit, the rest of the jaw structure has been reduced to beneath it.

Fig. 2.8 Top, shows the corrected jaw deformation when measured from different sections of the jaw structure, with Fig. 2.8 bottom showing where on the jaw those measurement is taken from. As can be seen in Fig. 2.8 most of the jaw structure has been corrected to below the 100 µm upper limit except for the absorber center line. This indicates potential localized deformation or mechanical separation within the jaw assemble that the ACS system cannot corrected for, but small discrepancies such as this could be corrected by the collimators fifth axis by moving the entire jaw laterally.

However, for the worst-case slow loss scenario, the addition of the actuator system to the jaw design has shown to have a positive effect on the correction of thermal deformations and reducing them by around a factor of five. Note: the apparent periodic change in the *absorber center line* plot in Fig. 2.8 (Top) is the localized deformations of the individual molybdenum carbide graphite absorption blocks.

2.3. PXI control system

Linking the actuation and the fiber strain measurement systems was a National Instruments® PXI closed loop controller. Light from the IFPI probes was recombined with the light from the reference arm of the interferometer (Fig. 2.2) and passed into a spectrometer based around a CMOS line array camera, in this case a Basler Racer raL8192-gm. As the intrinsic Fabry–Pérot interferometer is an absolute measurement system, at the start of operation the camera gave a value for the nominal condition of each optical fiber pair. This value was then carried over into the control part of the loop and formed the set point from which the magnitude of the corrective response was calculated. If no jaw deformation was occurring the set point (SP), and the reading from the optical fiber pair (PV), would remain the same. If deformation in the positive direction occurred so that PV increased, control would be applied. An output voltage proportional to the difference between SP and PV was outputted in the range of 0–10 V. This is then sent to the PZT amplifiers to be amplified proportionally from 0–10 V to 0–1000 V. If a negative displacement occurred so that PV decreased, no control will be performed. When the external stimulus was removed, and PV decreased back to the same value as SP, the proportional associated voltage would also be reduced allowing the jaw to relax into its nominal position.

3. Prototype and practical validation

Following on from the above series of FEA simulations, two full scale prototype adaptive collimator system (ACS) jaws were manufactured along with the all the supporting mechatronics and vacuum tank. This new prototype is shown in Fig. 3.1.
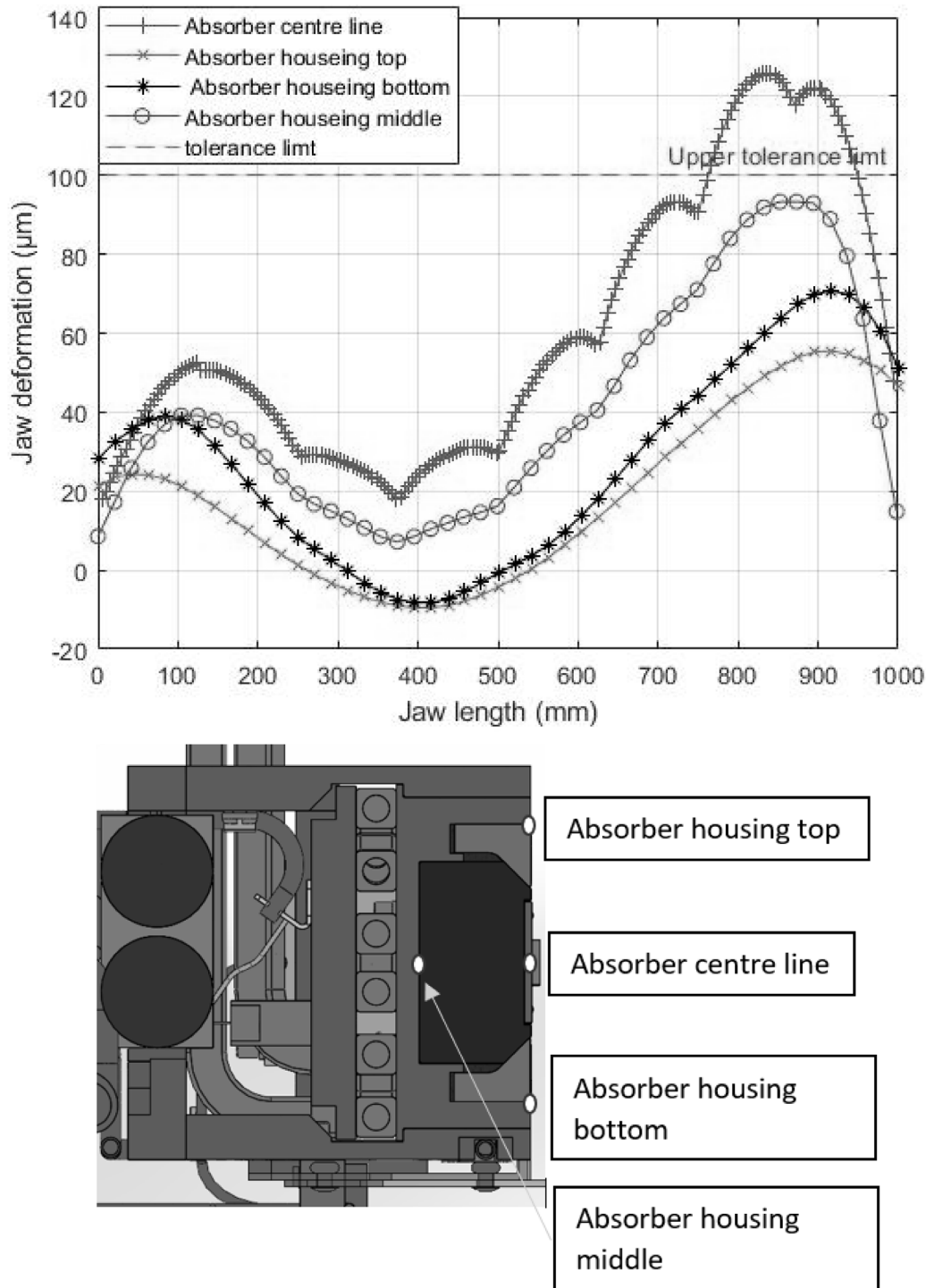
Fig. 2.8. (TOP) jaw deformations from several locations through jaw cross section (BOTTOM), showing the corresponding locations.

3.1. Jaw characterization

Before using the control system to monitor and correct jaw straightness, the system amplitude and hysteresis was checked. This was performed by using the PZTs to jog the jaw through the actuator system's full displaceable range. The displacement of the jaw was monitored by a dial test indicator (DTI) positioned at the center point of the jaw and all 6 fiber cavities frequencies captured in turn. Fig. 3.2 shows the slight hysteresis regarding the bend of the jaw when the actuators are subjected to the input voltage.

Fig. 3.2 shows that the control voltage has a reasonably linear response to bend and a sensitivity of 32.7 µm/V (input voltage). This is without any added DC offset or overcharging from the voltage amplifiers. Currently it is not known exactly what is causing the hysteresis in the jaw amplitude. Whilst there might be residual stiffness in the jaw body, more likely it is the dynamic hysteretic behavior of the PZT stacks. Hysteretic responses are intrinsic when using PZT actuators and is more prevalent when the stacks are exposed to additional stress and temperature [21].

Regarding the fiber measuring system, there is also some variation in the bi-directional results shown in Fig. 3.3 comparing the resultant
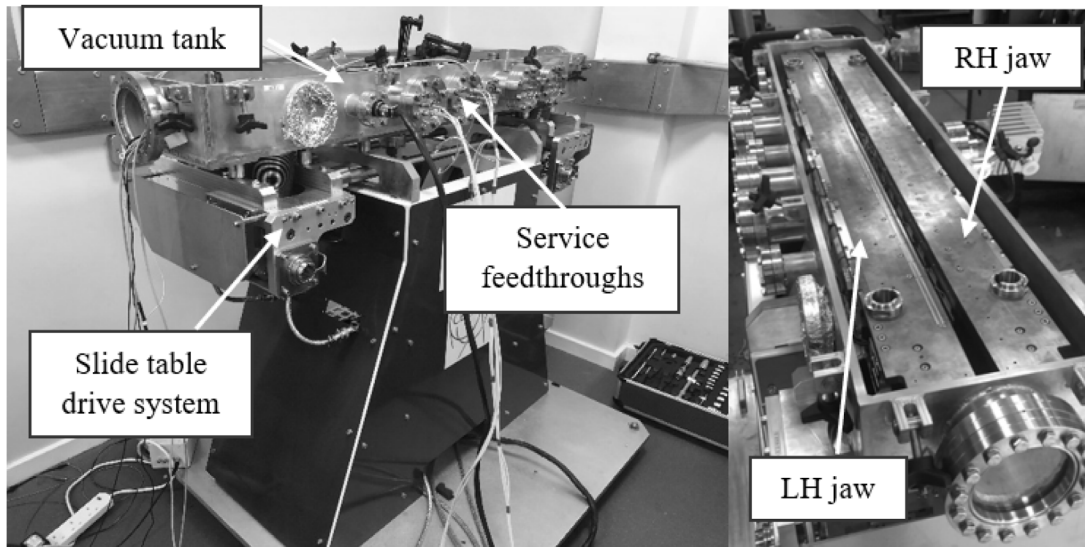
Fig. 3.1. ACS full size prototype collimator.
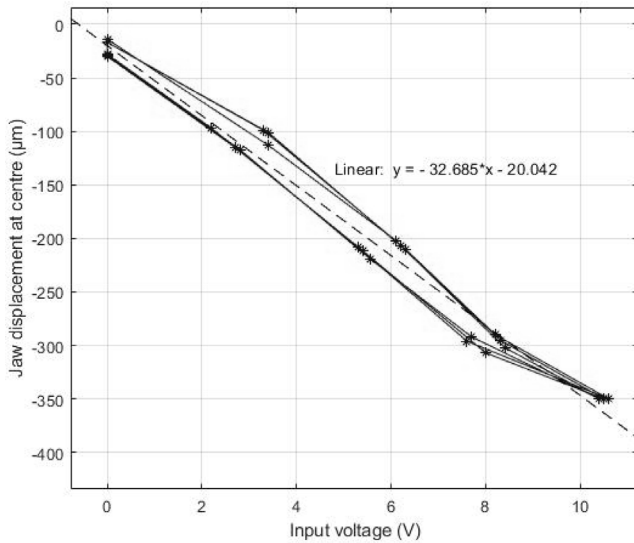

Fig. 3.2. Displacement vs. input voltage amplitude and corresponding hysteresis.

frequency change in the IFPI sensors compared to the jaw bend. This could indicate some hysteresis in the mechanical assembly rather than the piezo actuators. However, the results are more consistent and very linear. The average strain per micron bend in the front IFPI group is 0.00172 Hz/μm. As expected, the center fiber (Fiber 2) experiences greater strain than the side fibers (1 & 3). The difference in the side fibers is likely due to the small variation in preload due to assembly tolerances. The rear IFPI groups are under compression during actuation of the piezo system compared to tension at the front hence the change in gradient. The results show slightly more hysteresis when displaced compared to the front group, with an average strain per micron bend of 0.00205 Hz/μm. The strain values here are slightly higher due to their proximity to the piezo stacks which will cause some localized elongation when energized within the jaw in that area. All fiber positions in relation to the jaws geometry are shown in Fig. 3.5.

3.2. Static correction

To determine the ACS's actuation range and its ability to correct actual thermal deformations, as soon as the jaws were installed in the
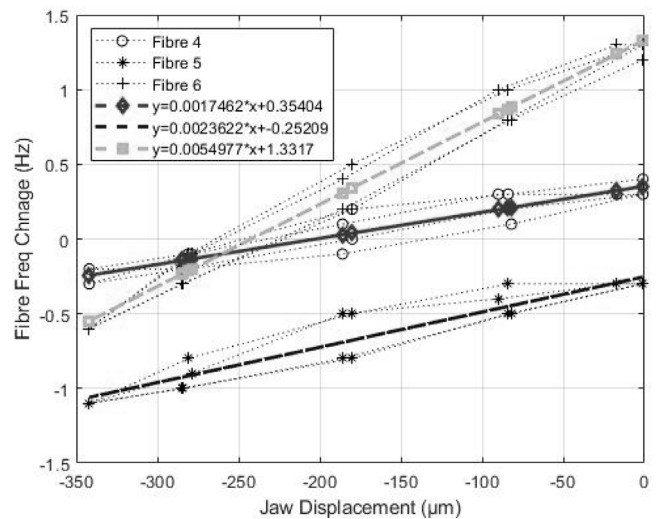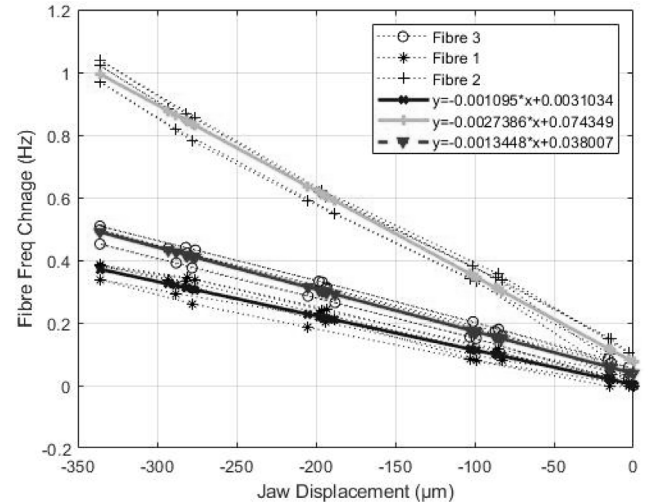

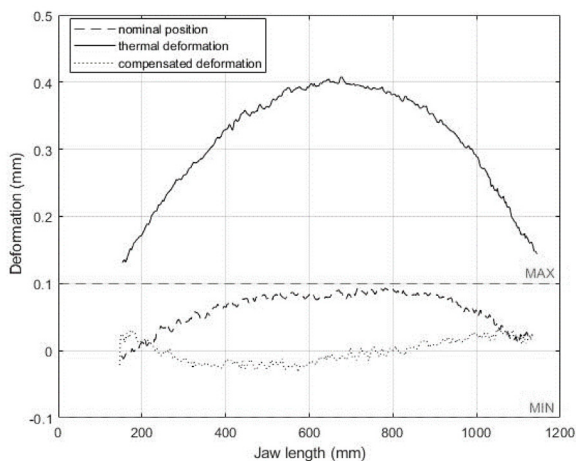**Fig. 3.3.** (Top) - front IFPI group hysteresis, (Bottom) -rear IFPI group hysteresis.

Fig. 3.4. (TOP) Romer arm being used to measure jaw straightness, (BOTTOM) jaw straightness results.

Fig. 3.5. Setup of adaptive control displacement test.

tank, the jaw's nominal straightness, thermally distorted straightness, and corrected straightness were measured using a Romer® Absolute portable CMM (Fig. 3.4 (top)). These straightness results are shown in Fig. 3.4 (bottom). As can be seen the jaw's nominal straightness (nominal position) is within the acceptable tolerance band of ±0.1 mm.

When activating the 16 TEC heaters embedded in the representative graphite absorption blocks, the combined 384 W of heating power raises the jaw's temperature to 79 °C (on the front face of the jaw) inducing as expected, a convex deformation "into the beam path" with a magnitude of 0.4 mm ("thermal deformation" Fig. 3.4 (bottom)). Also observed during this heating cycle there was a thermal induced twist of the entire jaw with respect to the datum point that was set when the jaw was at rest. This is illustrated by the apparent offset of the data with respect to zero. With the jaw's thermal deformation stabilized, 1000 V was passed across each of the eight PZT in induced the corrective movement. The "compensated deformation" in Fig. 3.4 show the jaw straightness after the corrective actuation has been applied and as can be seen the jaws resultant straightness is now inside the ±0.1 mm tolerance band.

Whilst the maxima of the thermal induced deformation were not as high as was simulated (519 μm from simulation), the overall corrective movement of the jaw was 426 μm. Therefore, it can be expected that during an actual 0.2 BLT scenario the actuation system would be able to reduce the jaws straightness error to below the upper tolerance limit.
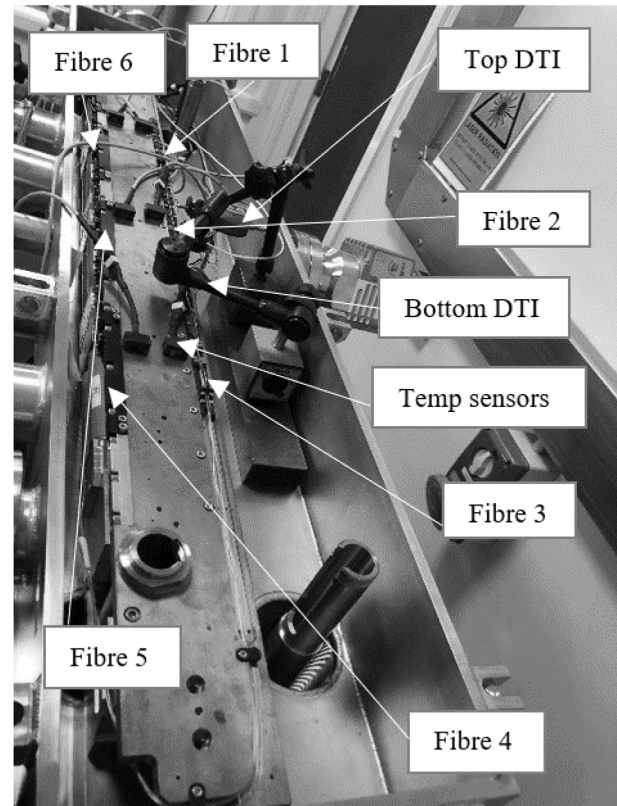
3.3. Slow adaptive control

For the adaptive control of these slow thermal deformations, the ACS's actuation system then was controlled automatically by measurement data sent back from the IFPI strain sensors via the National Instruments PXI system. In this test the deformation of the jaw was monitored by two digital displacement test indicators (DTI) placed on the top and bottom faces of the front part of the jaw. The temperature of the jaw was monitored by several temperature sensors placed on the jaw's top surface. This set up is shown in Fig. 3.5.

To determine a baseline measurement the jaw was heated for one hour, then monitored for an additional hour whilst cooling by natural convection. The observed deformation, temperature, and recorded front/back IFPI strain responses are shown in Figs. 3.6 and 3.7.

As can be seen in Fig. 3.6, at 55 °C the maximum deformation of the jaw is 0.2 mm. The difference in the top and bottom DTI readings is an apparent twist in the jaw structure as it deforms.

In Fig. 3.7 the front and back strain responses with respect to the jaws forward deformation can be seen, clearly showing a forward bend as the front IFPI group is straining more than the rear. However, there are two components that make up this response. The first is the strain the IFPI sensor undergoes due to bending deformation, and the second is the thermal elongation the sensor experiences due to the rising temperature of the whole jaw. The thermal effect of the fibers makes up a larger part of the recorded response than just the raw strain reading by itself. Efforts to use a separate sensor to solely capture the thermal effect temperature has on the IFPI sensors and subtract this value from the sensors monitoring jaw strain, were unsuccessful. The sensor being used to isolate the strain effect had to be mounted to the jaw in such a way that it would be subjected to the full amount of thermal conduction whilst not being affected by strain. However, the IFPI sensors are so sensitive that even just placing the fiber on the jaws top surface with
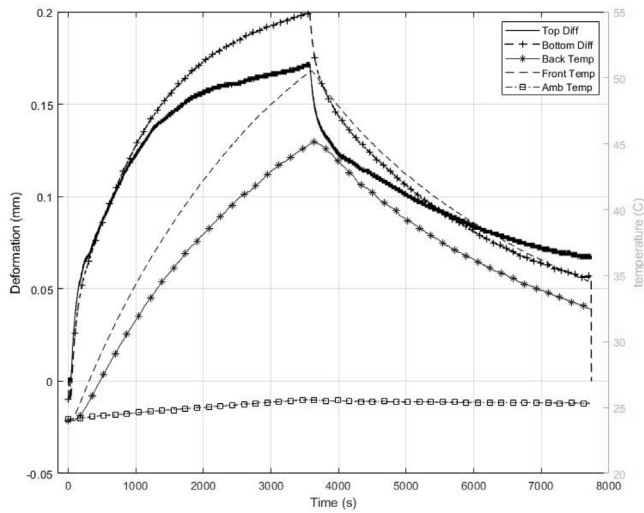
Fig. 3.6. Unconstrained deformation vs. temperature.

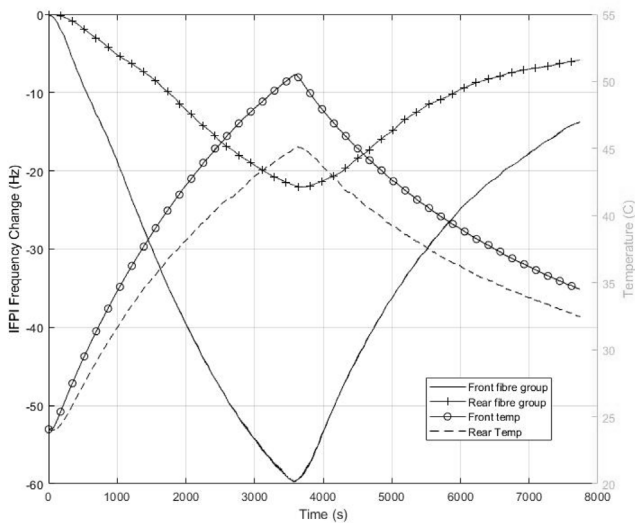**Fig. 3.8.** Controlled compensated deformation.

Fig. 3.7. Fiber response vs. temperature.

no additional constraint, the fiber would strain due to stiction between the fiber cladding and imperfections in the jaws surface.

The thermal effect on the fibers was therefore added into the control parameters because the combined temperature and elongations effects on the frequency change was still uniform, and there was still a noticeable difference between the front and rear fiber groups due to temperature and strain differences.

With this parameter added into the control system, the test was re-run but with the ACS compensation system activated. Fig. 3.8 shows the average controlled jaw deformation verses the nominal deformation when subjected to the same heat input.

As can be seen the actuation system has maintained the straightness of the jaw throughout the heating cycle between 0 and 0.1 mm.

Whilst the actuation system has sufficient force generation available to maintain the compensated deformation to a much lower magnitude, increasing the voltage output to bend the jaw as seen by the IFPI sensors causes a non-linear effect. Increasing the strain to bend variable taken from the jaw characterization to allow for a higher output voltage at the first stage of jaw deformation (0-1000s) would reduce this initial rise in deformation. However, this increased variable would lead to overcompensation later in the test (≈2000 s), overcompensating and
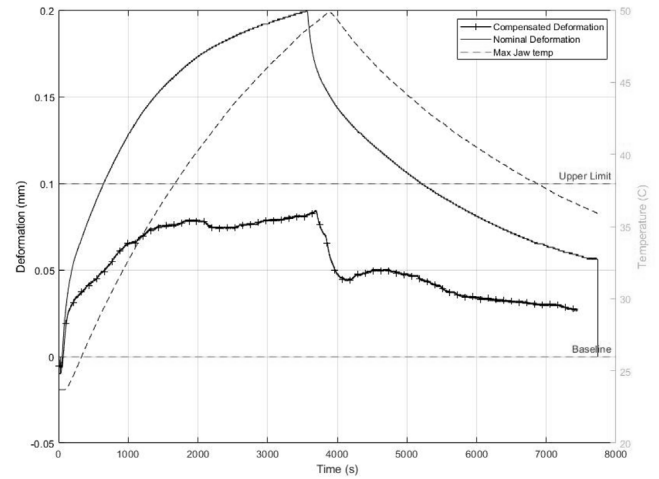
resulting on jaw deformation below the baseline. This effect is then further compounded when heating stops, as seen at T=3573 s. The abrupt halt to inputted heat power leads to a sudden drop in deformation magnitude. However, due to the thermal effect on the IFPI sensors, there is delay between the deformation dropping and the sensors seeing a drop in temperature. As there is no rapid drop in temperature, the IFPI sensors ensure that the actuation systems voltage is maintained. This continues until the sensors are affected by a temperature change, by which time they can allow the actuation voltage to be dropped.

By setting the strain to bend variable to those as seen in the jaw characterization section, with the addition of the thermal effect variable, the system can ensure that jaw straightness is kept between 0 and 0.1 mm for the duration of the heating and cooling cycle.

3.4. Consideration of thermal expansion

Initial tests using the slow thermal compensation system confirmed the secondary error component related to the piezo mounts and their longitudinal thermal expansion with the jaw. Fig. 3.9 shows the nominal deformation due to temperature and a preliminary compensation result. Whilst the compensated deformation is lower than the nominal, the deformation has exceeded the upper tolerance limit and the initial part of the deformation curve is almost identical to the nominal. This under compensation results from the difference between the bend/voltage calibration and the thermal expansion effects on the piezo mounts (preload).

Essentially, the longitudinal thermal expansion causes a non-linear separation of the actuator mounts compared to the piezo actuators. This effect was modeled in FEA and this separation distance was found to be 27 μm at a temperature of 50 °C. Given the system in its current configuration, and the variables relating strain to the actual bend and to the applied voltage, an additional 27 μm of elongation in the actuators could be achieved by proportionally applying approximately 1 V (PZT output equates 1 V to 33 μm of expansion) to the controllers output depending on the average of all the strain readings which effectively represents pure elongation. This proportionally applied 1 V ensured that the PZTs maintained the correct preload with their respective mounts throughout the duration of the test, leading to the results shown in Fig. 3.8.

3.5. Fast dynamic control

With the slow adaptive control primarily validated, the next phase of this investigation was to determine if the ACS could also mitigate
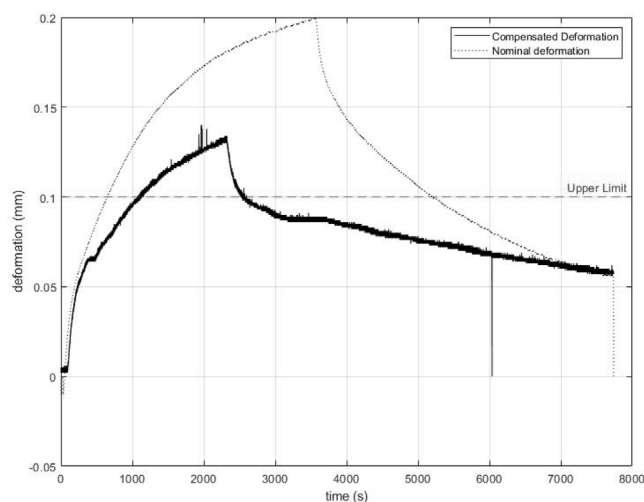
Fig. 3.9. Partially control deformation.

or dampen the vibratory effects generally associated with the dynamic losses, such as an accidental beam impact.

To account for slow changes in the sensor readings due to the aforementioned thermal distortion of the jaw, a variable reference was used for the high-speed control loop. A low pass filter was used to create a relatively slow-moving reference, any deviation from which was deemed to be a dynamic effect thereby triggering the dynamic control code in PXI control system. The standard deviation of the raw frequency data varies depending on the signal strength from the fibers, but it is typically 0.003 Hz. This translates to standard deviation of just under 2 μm in the amplitude of displacement at the center of the jaw, assuming a first order bend. The sampling rate of the control system is limited by the analog output of the NI PXI hardware which must be a 'on demand' configuration and is approximately 2200 Hz. This would indicate that the speed and resolution is sufficient to compensate for dynamic jaw deflection. However, the noise during control without any filtering did cause significant oscillation at the resonant frequency of the system of 51 Hz as indicated in the following results (Fig. 3.10).

Using a standard LabView PID controller, it was found that the output would drift because of the need to have the low frequency thermal control which means there was no fixed reference for the control. Using a simpler proportional controller based on the relative variations, the results varied substantially. Generally, the control would try to compensate but ultimately induced further vibration, hypothesized by means of the uni-directional actuation causing higher impact control actions at the zero crossing from negative bend (no compensation) to positive bend requiring full compensation.

To induce a vibratory response, a force hammer was used to strike the rear of jaw. This was done so that the correction would be in the direction correctable by the uni-directional actuation system. An independent reference in the form of an induction sensor was placed in front of the jaw to capture the resultant displacements. From several tests, results were gathered which initially demonstrated that the ACS could reduce the post-impact oscillations. An example of these results is shown in Fig. 3.11. However, in either case, the first peak which is the displacement from the initial impact from the hammer is not compensated, nor were all the subsequent oscillations.

To determine if additional filtering on the input signal from the fibers would help the responsiveness of the control system, the previous tests were repeated but using a softer tipped hammer. Using a softer tip would spread the hammers input energy over a much longer period allowing the control system more time to react which would potentially be needed if additional levels of low pass filtering were necessary. As can be seen in Fig. 3.12 adding this level of filtering to raw fiber output

signal does add a small delay to the buffer mean going to actuation system. This is highlighted by the two traces in Fig. 3.12 being slightly out of phase. However, with significantly more filtering to prevent the control output from changing faster than 50 Hz, slower changing impact deflection were successfully compensated (Fig. 3.13).

As can be seen in Fig. 3.13 the control system reduced the amplitude of the dynamic jaw displacement by an average of 70%. However, this was only observed when the rate of change in the displacement was quite low, equivalent to approximately 20 Hz, such that the extra phase shift caused by the filtering was relatively small but still managed to perform successful compensation. Although faster excitations were detected by the measurement system, rapid control movement excites the resonant frequency of the structure which the system feedback struggles to compensate with only the unidirectional actuation system. For soft hammer excitation where the impact is quite long the system compensates well, as shown in Fig. 3.13.

4. Conclusions & future work

This work has shown the hardware and software developments undertaken to generate a novel collimator design capable of monitoring and correcting thermal and vibratory deformations caused by beam/jaw interactions. From simulation it has been shown that the integration of the ACS actuation system into the jaw design can correct the deformations associated with the most challenging LHC design loss scenario that causes a dynamic deformation of the 1 m-long collimator jaw up to ≈0.5 mm. By producing a full-scale prototype and heating the jaw to artificially induce such first order deformation, the system achieved performance in good qualitative agreement with the simulated FEA results showing that this additional hardware can correct thermal deformations associated with these beam conditions. It has been observed that a total corrective displacement of 426 μm can be achieved using this system, which is enough to correct the 0.2 h BLT 500 μm thermal deformations to below the 100 μm tolerance limit. This system has also shown that it can maintain correction for these thermal deformations transiently for over one hour.

Additionally, this system has shown that it has the potential to dampen vibratory events, the type assorted with accidental beam impacts. More additional work is needed to reduce phase lag within the closed loop system, and whilst the force generation performed to induce vibratory responses was much lower than those found under actual beam conditions, this system did show amplitude reductions of 70% in the slow vibratory responses.

However, there are several areas that still require investigation to raise the technology readiness level of this concept. To ensure that actuation system response is proportional to the strain observed by the fibers, the thermal expansion of the fibers observed during the slow-loss heating tests needs to be decoupled in the resultant signal so that only fiber elongation due to strain is used. In addition, further investigation is required into a modified implementation of a PID control system for the fast frequency response. While the filtered proportional control worked well on slower period responses, a reduced phase delay is needed for the higher frequencies to reduce the faster vibratory responses. The current measurement system bandwidth and resolution should be more than adequate providing the uni-directional control (away from the beam) if it can be developed to work with limiting filtering.

In addition to the issues mentioned above there are several practical barriers to the use of technology that need to be resolved before it can used under beam conditions. For example, whilst the additional hardware (PZT's and IFPI probes) has been designed to be used in UHV environments, the ACS system as a whole still needs to be evaluated under UHV conditioned and under the associated bake out procedure that requires the collimator hardware to be heated to 250 °C for a protracted period. This is to ensure successful material outgassing's to allow for UHV compliance. The ACS functionality will need to be
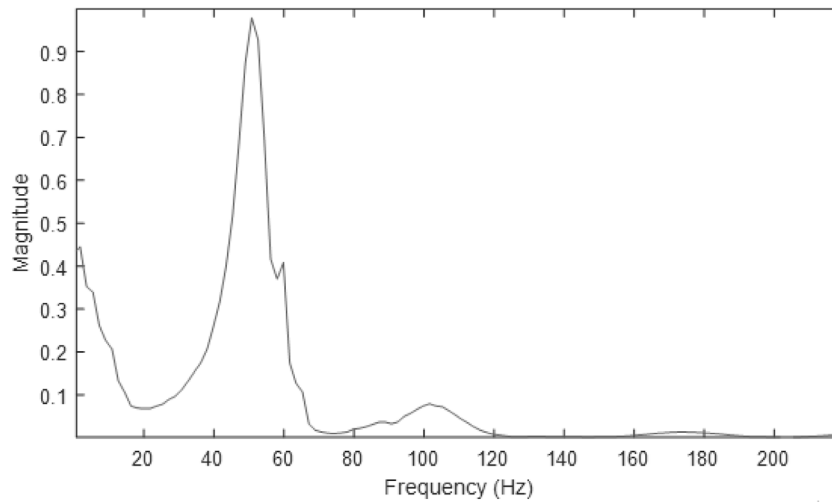
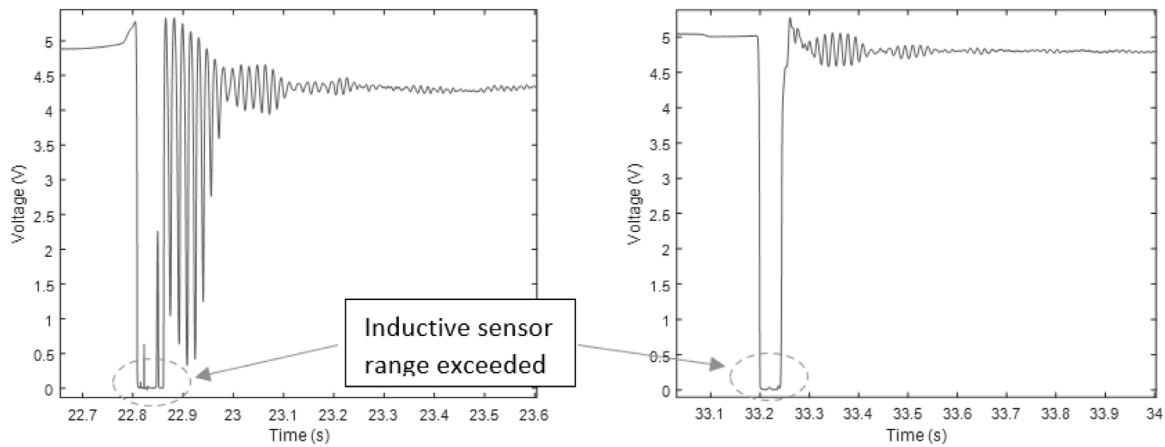**Fig. 3.10.** Power spectrum from FFT applied to inductive probe data taken during impact testing.

Fig. 3.11. Comparison of impact hammer responses from the reference induction sensor (LEFT): uncompensated, (RIGHT): compensated.
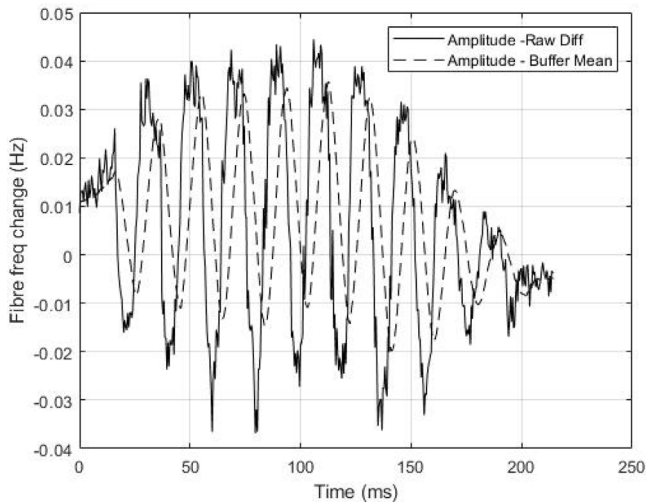

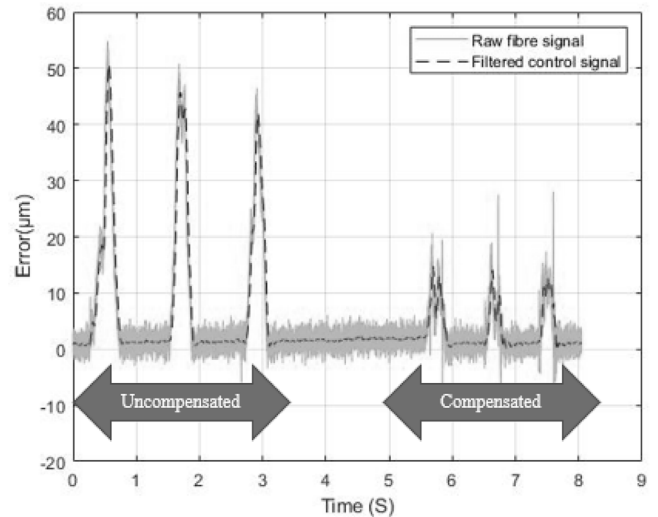**Fig. 3.12.** Resultant fiber frequency change - raw and filtered.

Fig. 3.13. Dynamic compensation results (triple impact), with and without compensation.

testing before and after such a bake out cycle to ensure consistent operation. The system also needs to be evaluated under prolonged radiological conditions. Whilst [10] details the work undertaken to ensure the IFPI probes are hardened against radiation darkening, and

to ensure maximum light transmission, this was done in isolation of the ACS system proper. Additional testing is required to determine the

control systems functionality and the functionality of the PZT stacks under the same levels of ionizing radiation.

Data availability

Data will be made available on request.

References

[1] R. Assmann, et al., The final collimation system for the LHC, in: Proceedings of EPAC, Edinburgh, 2006.

[2] F. Carra, et al., Mechanical robustness of HL-LHC collimator designs, in: 10th International Particle Accelerator Conference, Melbourne, 2019.

[3] E. Holzer, et al., Beam loss monitoring for LHC machine protection, in: TIPP 2011 - Technology and Instrumentation in Particle Physics 2011, Chicago, 2012.

[4] A. Bertarelli, et al., The mechanical design for the LHC collimators, in: Proceedings of EPAC 2004, Lucerne, 2004.

[5] T. Furness, et al., Adaptive collimator design for future particle accelerators, in: 7th International Beam Instumentation Conf., Shanghai, 2018.

[6] S. Redaeilli, R. Bruce, A. Lechner, A. Mereghetti, CERN Yellow Reports, HL-LHC Technical Report - Chapter 5, Collimation Systems, CERN, Geneva, 2020.

[7] A. Bertarelli, et al., Mechanical design for robustness of the LHC collimators, in: Proceedings of 2005 Particle Accelerator Conference, Knoxville, 2005.

[8] R. Schmidt, et al., Protection of the CERN large hadron collider, New J. Phys. 8 (2006) 1–31.

[9] R. Assman, et al., Requirements for the LHC collimation system, in: Eighth European Particle Accelerator Conference, EPAC, Paris, 2002.

[10] T. Furness, et al., In-situ displacement measurement for use in LHC collimators, in: Euspen's 20th International Conference & Exhibition, Geneva, 2020.

[11] F. Carra, Thermomechanical Response of Advanced Materials under Quasi-Instantaneous Heating (Ph.D. thesis), Politecnico di Torino, 2017.

[12] A. Mereghetti, et al., BLM thresholds and damage limits for collimators, in: 6th Evian Workshop on LHC Beam Operations, Evian Les Bains, 2015.

[13] F. Carra, et al., New TCSPM Design Compatility with HL Slow Loss Scenarios, CERN, Geneva, 2017.

[14] M. Cauchi, et al., Thermomechanical assessment of the effects of a jaw-beam angle during beam impact on large hadron collider collimators, Phys. Rev. Spec. Top. Accel. Beams 18 (2) (2015) 1–14.

[15] M. Cauchi, et al., Thermomechanical response of large hadron collider collimators to proton and ion beam impacts, Phys. Rev. Spec. Top. Accel. Beams 18 (4) (2015) 1–14.

[16] A. Ferrari, FLUKA: A Multi-Particle Transport Code (Program Version 2005), CERN, Geneva, 2005.

[17] G. Gobbi, B. Alessandro, F. Carra, J. Guardia-Valenzuela, S. Redaelli, Novel LHC collimator materials: High-energy hadron beam impact tests and nondestructive postirradiation examination, Mech. Adv. Mater. Struct. 27 (17) (2018) 1518–1530.

[18] A. Potdar, et al., Performance characterisation of a new photomicrosensor based sensing head for displacement measurement, Sens. Actuat. 238 (2016) 60–70.

[19] J. Williamson, A. Henning, H. Martin, T. Furness, S. Fletcher, X. Jiang, Flexible gauge length intrinsic fiber-optic strain sensor using broadband interferometry [invited], Opt. Image Sci. Vis. 37 (12) (2020) 1950–1957.

[20] PI, PI cermaic material data, 2018, [Online]. Available: https://static.piceramic.com/fileadmin/user_upload/physik_instrumente/files/datasheets/PI_Ceramic_Material_Data.pdf [Accessed 5 05 2018].

[21] N. Wongdamnern, N. Triamnak, A. Ngmjaurojana, Y. Laosiritaworm, S. Ananta, R. Yimnirun, Comparative studies of dynamic hysteresis responses in hard and soft PZT ceramics, Ceram. Int. 34 (1) (2008) 731–734.